Vacuum ultraviolet dielectric function of cubic InGaN for the entire composition range

Elias Baron [*] and Rüdiger Goldhahn
Institut für Physik, Otto-von-Guericke-Universität Magdeburg, Universitätsplatz 2, 39106 Magdeburg, Germany

Mario F. Zscherp, Silas A. Jentsch, Sangam Chatterjee, and Jörg Schörmann
Institute of Experimental Physics I and Center for Materials Research, Justus Liebig University Giessen, Heinrich-Buff-Ring 16, D-35392 Giessen, Germany

Natalia Nepomniashchaia and Alexandr Dejneka
Department of Optical and Biophysical Systems, Institute of Physics of the Czech Academy of Sciences, Na Slovance 2, Prague 18221, Czech Republic

Martin Feneberg
Institut für Physik, Otto-von-Guericke-Universität Magdeburg, Universitätsplatz 2, 39106 Magdeburg, Germany

(Received 19 March 2026; accepted 19 August 2026; published 14 September 2026)

The cubic zincblende polymorph of InGaN is a very promising candidate for optical applications. Its absence of spontaneous polarization fields in the (001) orientation and lower fundamental band gap compared to its wurtzite counterpart makes it especially interesting for efficient light-emitting diodes (LEDs) and micro-LEDs. Therefore, understanding the optical properties and band structure of this material plays a key role in the development of possible future applications. For this, the current study presents the optical properties in the form of the dielectric function of thin film $In_xGa_{1-x}N$ for entire composition range ($0 \leqslant x \leqslant 1$). The investigated spectral regions range from the near-infrared (0.5 eV) to the vacuum ultraviolet (8.8 eV). We focus on the spectral ranges above 4 eV to study the redshift of the higher energy transition (E_1 at the L-point of the band structure and E_2 at the X-point) as the In composition changes from GaN to InN. The characteristic energy of these transitions at critical points in the band structure are determined by a critical point model based on the third derivative of the dielectric function. Bowing fits of the E_1 and E_2 transitions yield bowing parameters of $b_1 = 1.01$ eV and $b_2 = 0.50$ eV. Furthermore, we determined the dielectric limit as $\varepsilon_\infty = \varepsilon_1(E \to 0)$, yielding a bowing parameter of $b_\infty = 1.58$.

DOI: 10.1103/d9pn-bys3

I. INTRODUCTION

The well-known and well-established group-III nitrides, used in optoelectronics [1–4] and power devices [5–8], normally crystallize in the hexagonal wurtzite phase. However, they also possess a metastable [9] cubic zincblende phase, which can be achieved under special growth conditions [10]. These cubic polymorphs of gallium nitride (c-GaN), indium nitride (c-InN), and aluminium nitride (c-AlN), as well as their alloys, are promising candidates for certain applications like quantum devices [11–13]. They may also outperform or replace their wurtzite counterparts in special cases [14–17]. Most notably for this is the possibility of cubic nitrides in light-emitting diodes (LEDs) based on quantum wells [18–23]. Here, the absence of internal polarization fields of cubic nitrides in (001) orientation [18,24] improves efficiency by preventing losses due to quantum-confined Stark effect, which occur in the wurtzite phase [25–28]. Furthermore, especially considering LEDs based on InGaN for light emissions in the red to green spectral ranges, the lower fundamental band gaps of cubic nitrides means less indium incorporation to achieve the target wavelength.

The cubic AlGaN system (including the binary compounds) has been studied earlier, both experimentally and theoretically, for the entire aluminium composition range [29–34]. For a long time, cubic $In_xGa_{1-x}N$ (c-InGaN) of good crystal quality was limited to In contents x below 0.3 due to such problems as different lattice constants and growth temperatures or decomposition. However, recent progresses in growth and control, like sophisticated strain management, allowed for growth of phase-pure material over the entire indium composition range [35]. Further improvements on crystal quality and emission efficiency generates more interest in these systems [22,36–38].

The comprehension of optical properties over a wide spectral range is not only significant for optical applications, but

[*]Contact author: elias.baron@ovgu.de

also for understanding the electronic band structure. Comparing experimental results with band structure calculations is a vital part in this. While synchrotron based experiments or similar setups determine the optical properties up to 20 [30,31,39] or even 40 eV [40], even measurements in the vacuum ultraviolet (VUV) can provide valuable insights [29,41,42], especially for lower band gap materials. This was performed earlier for wurtzite InGaN [43], which gives a nice comparison for the current work. Based on band structure calculations [44,45] for the binary endpoints c-GaN and c-InN, both materials display optical transitions in the VUV spectral range: the E_1 transition at the L-point and the E_2 transition at the X-point of the Brillouin zone.

Recently, we published a study [46] investigating and analyzing the absorption edge shift due to indium alloying from c-GaN ($E_G^{GaN} = 3.23$ eV [31,33]) to c-InN ($E_G^{InN} = 0.60$ eV [46–48]). There, we additionally accounted for free-carrier contributions and strain effects on the band gap. This leads to the conclusion of a band gap bowing with a bowing parameter of $b_G = 1.61$ eV [46]:

$$E_G^{InGaN}(x) = xE_G^{InN} + (1-x)E_G^{GaN} + x(x-1)b_G. \quad (1)$$

This equation will also be used in this study to determine the dependence of higher energy transitions as well as the dielectric limit on the In content, by replacing E_G by E_1, E_2, and ε_∞, respectively.

In the current study, we explore the higher energy transitions of thin film c-$In_xGa_{1-x}N$ by means of spectroscopic ellipsometry for $0 \leqslant x \leqslant 1$. For this, we determine the complex dielectric function (DF) $\varepsilon = \varepsilon_1 + i\varepsilon_2$ from the near infrared (NIR) to the VUV with a focus on photon energies above 4 eV. The characteristic energies of optical transitions at critical points (CP) of the band structure are obtained by utilizing a CP model. Furthermore, we perform bowing fits on two of the three observed transition energies. Additionally, the dielectric limit is investigated as well and also described by a bowing fit.

II. EXPERIMENTAL

In this study, we investigate thin-film c-InGaN samples deposited by plasma-assisted molecular beam epitaxy on a 3C-SiC/Si (100) substrate [35,46]. For better crystal quality, c-GaN/c-AlN buffer layers were deposited before the c-InGaN layer [49]. The sample structure is shown in Fig. 1. Different samples contain varying In content x as well as different c-InGaN layer thicknesses. While the In content was determined by high-resolution x-ray diffraction (HRXRD), the c-InGaN layer thickness was determined by spectroscopic ellipsometry. Detailed sample parameters can be found in our previous studies [35,46]. However, a brief summary of selected parameters is given in Table I. For easier comparability, we have chosen the same sample names as in our previous study [46]. Unfortunately, we were unable to properly analyze samples B and D from that study. Therefore, they are not included here.

We employed two different ellipsometers with overlapping spectral ranges for the optical characterization from the NIR to the VUV. A Woollam VASE obtained the optical data from 0.5 to 6.5 eV, while a Woollam VUV-VASE (spectral range: 0.8−8.8 eV) was used for the extension up to 8.8 eV. All

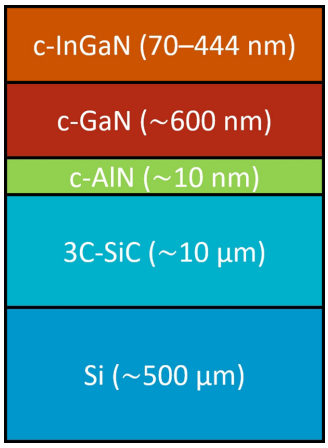

FIG. 1. Principle sample structure of the investigated samples. Sample A (see Table I) does not contain the top-most c-InGaN layer. All layers possess the (001) orientation.

measurements were performed at room temperature for three different angles of incidence: 50°, 60°, and 70°.

Our analysis starts by fitting a layer model, based on the sample structure given in Fig. 1, onto the ellipsometric angles Ψ and Δ. This layer model also includes a surface roughness layer at the top by means of effective medium approximation (EMA) using Bruggeman's formalism [50]. For this, we assumed a percentage of voids in a layer of c-InGaN. Both the thickness of this surface roughness layer and the void percentage were fitting parameters. (A comparison between surface roughnesses determined by ellipsometry and atomic force microscopy can be found in Sec. S1 in the Supplemental Material [51].) Within the layer structure, we use model-DFs containing modified versions of the general Herzinger-Johs parametrized semiconductor oscillator functions (PSEMI) [52,53] based on our previous results on the

TABLE I. Selected sample properties: In content x determined by HRXRD, thickness of the c-InGaN layer (d_{SE}), thickness of the surface roughness layer (d_{rough}), percentage of void in the surface roughness (EMA), optical free-carrier concentration (n_{opt}), optical transition energy (E_{CV}) determined by spectroscopic ellipsometry, and calculated fundamental band gap (E_G). All values (except d_{rough} and EMA) as well as the sample names are taken from our previous study [46].

Sample	x	d_{SE} (nm)	d_{rough} (nm)	EMA (%)	n_{opt} (10^{19} cm^{-3})	E_{CV} (eV)	E_G (eV)
A (c-GaN)	0.00	557	2	50		3.23	3.23
C	0.11	81	4	76	1.06	2.85	2.79
E	0.16	361	13	63	2.49	2.71	2.60
F	0.23	94	4	78	2.21	2.47	2.33
G	0.28	444	14	82	2.51	2.34	2.19
H	0.32	80	6	65	2.10	2.16	2.00
I	0.45	70	8	77	2.11	1.84	1.67
J	0.55	102	13	77	2.09	1.53	1.35
K	0.67	104	9	86	1.68	1.33	1.15
L	0.88	106	6	73	2.05	1.07	0.78
M (c-InN)	1.00	98	10	85	2.43	1.01	0.60

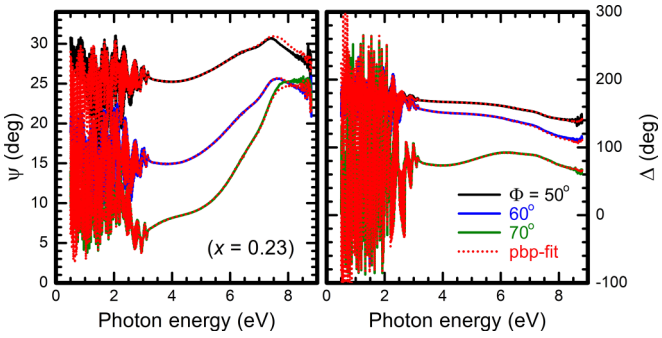

FIG. 2. Measurement data for three different angles of incidence (continuous curves, black 50°, blue 60°, and green 70°) and point-by-point fit (pbp-fit, red dotted) for sample F. The high frequency Fabry-Pérot oscillations below 3.2 eV (absorption edge of c-GaN) overlap between each curve.

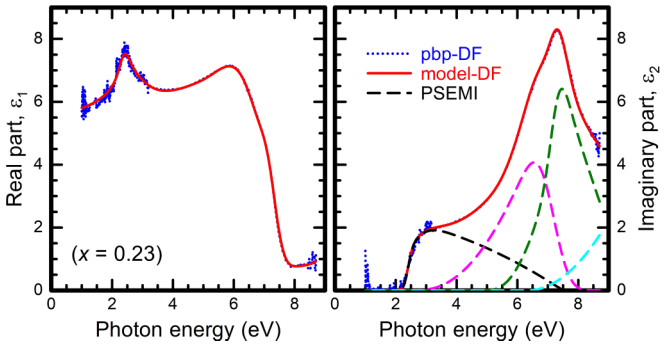

FIG. 3. Point-by-point dielectric function (pbp-DF, blue dotted) and model dielectric function (model-DF, red continuous) fitted onto the pbp-data for sample F. The model-DF consists of four PSEMI oscillators (only shown for the imaginary part, dashed curves, black for PSEMI-M0; and pink, green, and cerulean for PSEMI-M1), representing the optical transitions at critical points of the band structure as well as a higher energy contribution.

optical properties of c-InN [48], c-GaN [31,33], and c-AlN [30], as well as c-InGaN [46]. The optical properties of the substrate can be found elsewhere [54–57]. This initial fit, based on a least mean square algorithm, provides information about thicknesses and surface roughness contributions, the latter of which are given in Table I. However, we did not obtain any parameters of the DF from this fit. After a good agreement between layer model and measurement data was achieved, we proceeded with a point-by-point (pbp) fit, which changes the optical constants of the model c-InGaN layer wavelength by wavelength to fit the optical data. From this, we obtained the pbp-DF. The line shape of this pbp-DF is then described by a model-DF containing different PSEMIs. Which PSEMI is used for what transition in the pbp-DF will be discussed in the next section. The material parameters obtained by this PSEMI-based model-DF could be used, however, we apply a more accurate CP model on the pbp-DFs to get a more accurate determination of the CP energies. For this, we calculate the third derivative of the pbp-DF multiplied by E^2 and fit the following model onto it [58–60]:

$$\frac{d^3}{dE^3}(E^2\varepsilon) = \sum_j \frac{C_j e^{i\Phi_j}}{(E - E_j + i\Gamma_j)^3}. \tag{2}$$

Here, j is the number of CPs used in the fit, while C_j, Φ_j, E_j, and Γ_j resemble the amplitude, phase, energy position, and broadening of the jth CP, respectively. We assume the higher energy transitions investigated in this study to be M1-CPs with a dimensionality of 2, which leads to the exponent 3 on the right side of Eq. (2) [60]. Although we use the third derivative in this study to obtain the energy positions, we also tried the analysis with the second derivative (see S6 in the Supplemental Material [51]). Here, we obtained similar values. However, using the third derivative led to more systematic results overall.

III. RESULTS

We begin by examining the combined experimental data of both ellipsometers for a selected sample. For this, we decided to display Ψ and Δ for the three angles of incidence as well as the pbp-fit for sample F in Fig. 2. Here, the spectrum is dominated by strong Fabry-Pérot oscillations below 3.2 eV, which vanish at the band gap of c-GaN. These oscillations, due to thin film interference of mainly the 3C-SiC and c-GaN layers, can have strong impacts on the pbp-fit if not properly accounted for in the layer model. This is especially problematic for samples with high In content and a thin c-InGaN layer ($d_{SE} < 100$ nm). In this case, the fundamental band gap of c-InGaN is even below the indirect band gap of 3C-SiC (2.4 eV) and the low c-InGaN layer thickness enables much of the incoming light to reach the lower layers. This partial transmission can increase parameter correlation between thickness and the retrieved DF, which can locally reduce the robustness of the fit below 3.2 eV. All of this makes the analysis of the absorption edge region much more difficult. However, since we already discussed this in our previous study [46], we will mainly focus on the higher energy transitions (above 4 eV) where the absorption of the c-InGaN layer is strong enough to prevent signals from lower layers and the DF becomes much less sensitive to interference effects. In this spectral region, the pbp-fit yields a great agreement with the experimental data, except for a slight mismatch around 8 eV in Ψ for 50° and 70°. Nevertheless, a mean squared error (MSE) of 3.861 was achieved. No smoothing procedures were performed to either the experimental data or the pbp-fit results in any analysis. (The pbp-fit for all samples can be found in Secs. S2–S4 in the Supplemental Material [51].)

The resulting pbp-DF was extracted and displayed in Fig. 3. Here, the fit by a model-DF based on PSEMIs is shown as well. For this, we chose four PSEMI oscillators: one PSEMI-M0 for the absorption edge at ∼2.4 eV, two PSEMI-M1 for the following transitions at ∼6.6 eV and ∼7.3 eV, as well as one additional PSEMI-M1 for even higher contributions, outside of the spectral range. The pbp-DF contains some noise below 3.2 eV due to the aforementioned Fabry-Pérot oscillations. Nevertheless, a great agreement between pbp- and model-DF was achieved for both real and imaginary part, with a MSE of 0.101.

The same procedure was performed for all samples. However, an additional PSEMI-M1 oscillator was used for an

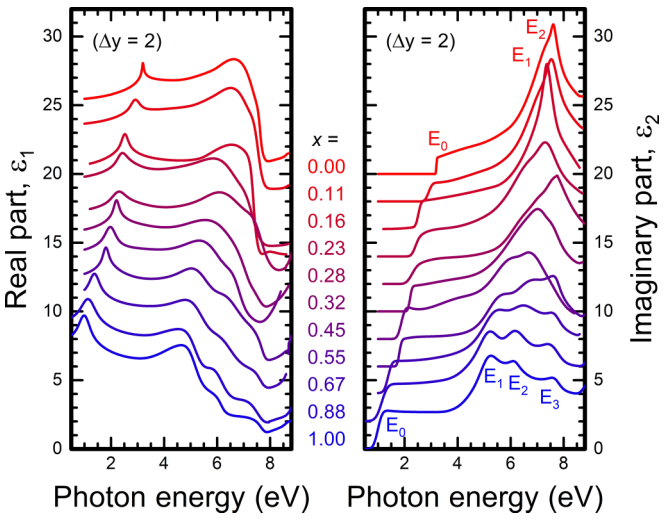

FIG. 4. Model dielectric functions (model-DF) for all samples from c-GaN (red, at the top) to c-InN (blue, at the bottom). These model-DFs consist, for c-GaN-like samples, of four PSEMI oscillators (E_0, E_1, E_2, and higher contributions outside the spectral range) like shown in Fig. 3. For c-InN-like samples, five PSEMI oscillators were used, due to an additional optical transition (E_3) signal around 7.6 eV. Between each curve is a vertical shift of 2. The In content x is given at the center in the appropriate color. The pbp-DFs are not shown for better visibility.

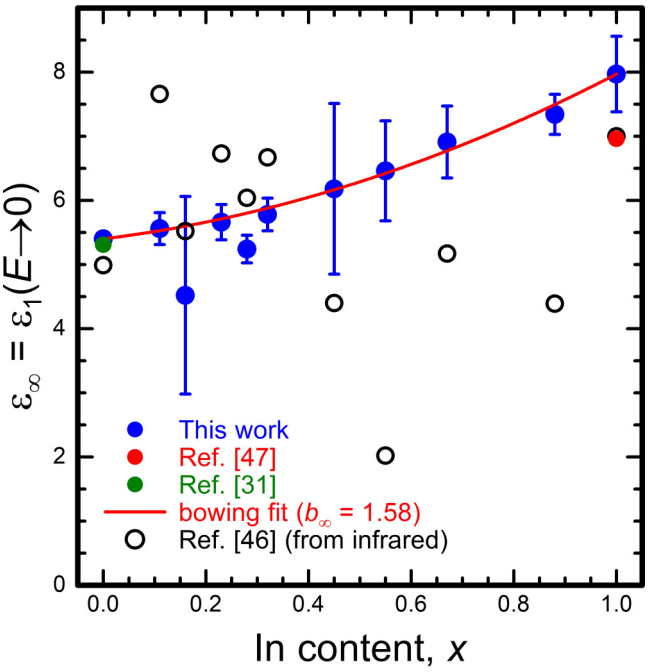

FIG. 5. Dielectric limits for all samples as well as the corresponding bowing fit. Samples E ($x = 0.16$) and G ($x = 0.28$) are excluded from the bowing fit, due to the large difference compared to the trend of the other samples. The dielectric limits are determined as the extrapolation of the PSEMI models in Fig. 4 for $\varepsilon_1 \to 0$.

emerging third transition around 7.6 eV for samples with an In content above 0.23. The results of the fitted model-DFs are shown in Fig. 4 for all samples. For some samples, depending on the c-InGaN-layer thickness, the pbp-DFs is very noisy around the absorption edge (see our previous publication [46]) due to the Fabry-Pérot oscillations. Therefore, we decided to not display the pbp-DFs for better visibility of the overall change of the DF with In content. However, the agreement between model-DF and pbp-DF above 3.2 eV is of the same quality as shown in Fig. 3 for each sample. (The fit of the model-DF onto the pbp-data for all samples can be found in Sec. S5 in the Supplemental Material [51].) The line-shape differences for $x = 0.16$, 0.28, and 0.45 could result from the small deviations in the pbp-fit for energies greater than 7 eV. Furthermore, the line-shapes display slightly different behaviors than theoretical predictions on the DF of c-InGaN, although the dominant E_2 is represented well [61]. The spectral absorption coefficients calculated by these DFs yield a characteristic absorption depth of less than 60 nm for all c-InGaN samples above 4 eV, meaning that for these spectral ranges we mainly penetrate the c-InGaN layer only.

We extrapolated the model-DF for each sample to obtain the dielectric limit $\varepsilon_\infty = \varepsilon_1(E \to 0)$. This means that no single PSEMI parameter is used to determine ε_∞. The results are displayed in Fig. 5 as well as Table II. The given error bars are taken from the fitting errors of the model-DF fit on the pbp-data. A bowing fit between the values for c-GaN and

TABLE II. Results from the PSEMI- and CP-model analysis for each sample: dielectric limit ε_∞ and energy values for the higher energy transitions (E_1 at the L-point of the band structure, E_2 at the X-point and E_3). The values marked with * are not included in the respective bowing fits.

Sample	x	ε_∞	$E_1(L)$ (eV)	$E_2(X)$ (eV)	E_3 (eV)
A	0.00	5.40 ± 0.02	7.45 ± 0.01	7.68 ± 0.01	
C	0.11	5.56 ± 0.25	7.21 ± 0.06	7.57 ± 0.01	
E	0.16	4.52* ± 1.54	7.05 ± 0.09	7.38 ± 0.01	
F	0.23	5.66 ± 0.28	6.90 ± 0.01	7.37 ± 0.01	7.83 ± 0.03
G	0.28	5.24* ± 0.22	6.60 ± 0.04	7.57* ± 0.10	7.76 ± 0.01
H	0.32	5.78 ± 0.26	6.61 ± 0.04	7.26 ± 0.06	7.77 ± 0.03
I	0.45	6.18 ± 1.33	5.68 ± 0.18	6.64 ± 0.03	7.28 ± 0.26
J	0.55	6.46 ± 0.78	6.08 ± 0.05	6.68 ± 0.05	7.74 ± 0.01
K	0.67	6.91 ± 0.56	5.48 ± 0.08	6.62 ± 0.03	7.76 ± 0.01
L	0.88	7.34 ± 0.31	5.11 ± 0.04	6.27 ± 0.01	7.77 ± 0.01
M	1.00	7.97 ± 0.59	5.04 ± 0.04	6.19 ± 0.01	7.76 ± 0.01

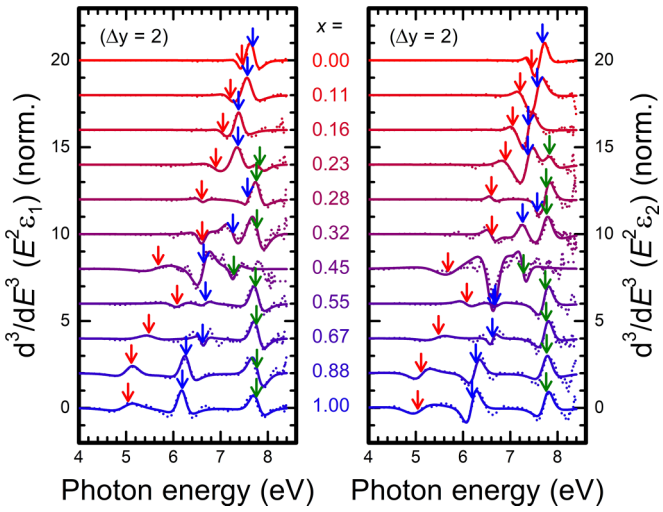

FIG. 6. Third derivative of the point-by-point dielectric functions multiplied by E^2 (dotted curves) for all samples as well as the corresponding critical point model fits (continuous curves). Each curve was normalized to its maximum and vertically shifted by 2 compared to the previous curve. The In content x is given at the center in the appropriate color. Arrows indicate the characteristic energies for the E_1 (red), E_2 (blue), and E_3 (green) transitions, as determined by Eq. (2).

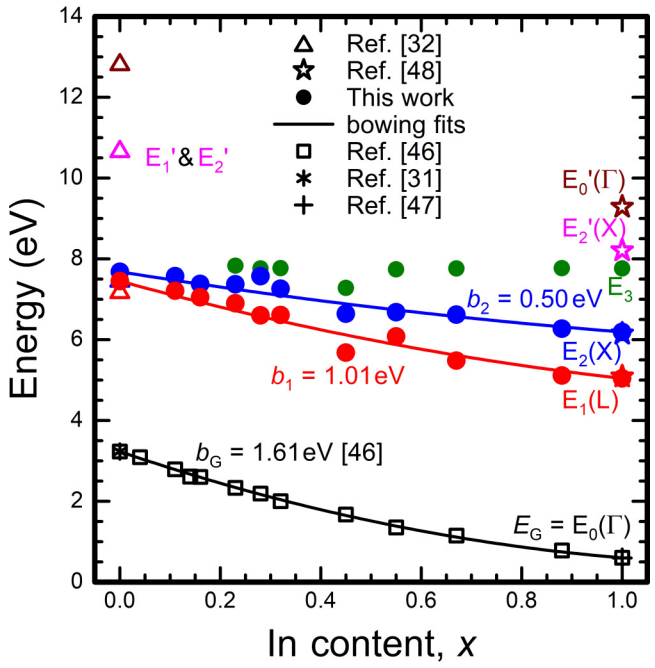

FIG. 7. Transition energies (red E_1 at the L-point, blue E_2 at the X-point, and green E_3, which is not yet clearly identified) determined by critical point model fits for all samples. The E_3 transition was not visible for samples with $x < 0.23$. The error bars for the transition energies determined in this work are too small to be visible at this scale. Additional transitions from literature [32,48] (pink and brown), as well as our previously determined absorption edge analysis [46] (black) are displayed for comparison. The E_1' and E_2' transitions in c-GaN ($x = 0$) occur at the same energy [32]. Bowing fits (dashed) with their respective bowing parameters b are displayed for the E_1 and E_2 transitions as well as for the band gap. The E_2 value for $x = 0.28$ was not included into this fit.

c-InN yields a bowing parameter of $b_\infty = 1.58 \pm 0.16$. For this bowing fit, the samples E and G were excluded, leading to a MSE of 0.007.

The model-DFs displayed in Fig. 4, obtained by PSEMI oscillators, were only used to represent the line shape of the pbp-DF and determining the dielectric limit. The characteristic energies of the CPs are determined by a fit of the CP model [Eq. (2)] to the third derivative of the pbp-DF, not the model-DF. We obtain this derivative by locally fitting a third-order polynomial to the pbp-data with a fixed interpolation width of 51 points. Since we are only interested in the higher energy transitions, because the band gap region was already analyzed in our previous study [46], the CP-model fits can only be seen for the optical data above 4 eV in Fig. 6. Here, a great agreement between the CP model and the third derivative of the pbp-DF is achieved. The analysis of c-GaN ($x = 0$) and low In content samples yielded only two CPs, while three CPs were needed for samples with $x > 0.2$. This reinforces our approach of using the CP-model analysis, since the third transition was not visible in the PSEMI analysis for sample F. The characteristic energy may not always be at the same line shape position (e.g., not always at the maximum) for each sample and CP, due to the freely fitted phase parameter in Eq. (2), which can account for effects like surface electric fields.

The determined energies for the high-energy CPs of all samples are shown in Fig. 7 as well as in Table II. (The other CP-model parameters are displayed in Sec. S7 in the Supplemental Material [51].) Additionally, we display the band gap analysis from our previous study [46] as well as even higher CP transitions for c-GaN [32] and c-InN [48] for comparison. Based on band structure calculations [44,45], we attribute the two high-energy CPs in c-GaN (at 7.45 eV and 7.68 eV) to the E_1 and E_2 transitions, located at the L- and X-points of the Brillouin zone, respectively. The same assignment is true for the 5.04 eV and 6.19 eV transitions in c-InN. These values are in good agreement with theoretical calculations [61]. We performed bowing fits [see Eq. (1)] to these E_1 and E_2 transitions yielding bowing parameters of $b_1 = 1.01 \pm 0.33$ eV and $b_2 = 0.50 \pm 0.21$ eV. There is clearly one outlier for the E_2 transition at $x = 0.28$, which was omitted for the bowing fit. With this, MSE values of 0.035 and 0.013 were achieved for the E_1 and E_2, respectively. The values of the bowing parameters are lower compared to the respective values in wurtzite InGaN of $b_1^{wz} = 1.07$ eV and $b_2^{wz} = 1.03$ eV [43]. The fact that the higher energy transitions display smaller changes with In content was also reported for other ternary systems earlier [32,62–64].

The third transition in c-InN, at 7.76 eV, is not yet exactly classified, because this signal does not appear to shift with the In composition, but is clearly observed until $x = 0.23$. Further investigations and comparison with similar samples are needed. For the context of this study, we name the 7.76 eV signal as E_3. The next higher transition in literature would be the E_2' transition into the next higher conduction band, the X-point. This, however, is usually at even higher energies [31,32,48]. Looking at the theoretical band structures [44,45],

the K-point transition seems to fit the signal better energetically. However, comparing the other cubic nitrides as well as arsenides and phosphides, a K-point transition seems unlikely as it is normally not observed [31,32,48,59,65–67]. Another explanation could be inclusions of wurtzite InN, since the extraordinary DF does display a T_2 transition at this energy [48]. However, a reciprocal space map analysis of these samples, measured by means of high-resolution x-ray diffraction, does not show any significant wurtzite inclusion [35]. Furthermore, we would expect additional contributions of these wurtzite inclusions at other spectral regions, for example in the band gap region, as well.

IV. SUMMARY

In this study, we have investigated the optical properties of cubic InGaN thin films over the entire composition range. The samples were grown by plasma-assisted molecular beam epitaxy on c-GaN/c-AlN buffers on 3C-SiC/Si substrates, all oriented in the (001) direction. Utilizing spectroscopic ellipsometry from the NIR to the VUV spectral ranges, we determined the optical properties in form of the DF by means of a pbp-fit and described the line-shape by a sum of PSEMI oscillators. We were able to determine dielectric limits ε_∞ by extrapolating the PSEMI model for each sample. The dependence on the In content was described by a bowing fit with $b_\infty = 1.58$. Furthermore, we analyzed the higher energy transitions E_1 and E_2 at the L- and X-point of the band structure, respectively, as well as a third transition E_3 by performing CP-model fits onto the third derivative of the product of pbp-DF and E^2. The bowing fits of the E_1 and E_2 transitions yield bowing parameters of $b_1 = 1.01$ eV and $b_2 = 0.50$ eV, which are smaller than their wurtzite counterparts. It remains unclear the apparent independence of the E_3 transition on the In content. Further investigations will reveal the exact identity of this transition.

ACKNOWLEDGMENTS

We gratefully acknowledge support through the European Regional Development Fund (ERDF) for the project "Innovationslabor Prozessdiagnostik" under Contract No. 21031934. S.C. acknowledges funding through the State of Hesse Landes-Offensive zur Entwicklung Wissenschaftlich-ökonomischer Exzellenz (LOEWE) by the Transfer-Professur "Hochtechnologiematerialien".

DATA AVAILABILITY

The data that support the findings of this study are available from the corresponding author upon reasonable request.

[1] C. J. Praharaj, *Group III-Nitride Semiconductor Optoelectronics* (John Wiley & Sons, Inc., Hoboken, NJ, 2024).

[2] J. Min, Y. Wang, T.-Y. Park, D. Wang, B. Janjua, D. Jeong, G. S. Kim, H. Sun, C. Zhao, J. C. Mendes, M. R. P. Correia, D. F. Carvalho, J. P. S. Cardoso, Q. Wang, H. Zhang, T. K. Ng, and B. S. Ooi, Bottom-up formation of III-nitride nanowires: Past, present, and future for photonic devices, Adv. Mater. **36**, 2405558 (2024).

[3] J.-H. Park, M. Pristovsek, C. Wentao, T. Kumabe, S.-Y. Choi, D.-S. Lee, T.-Y. Seong, and H. Amano, Droop and light extraction of InGaN-based red micro-light-emitting diodes, Semicond. Sci. Technol. **39**, 01LT01 (2024).

[4] T. Fujisawa, N. Hu, T. Kojima, T. Egawa, and M. Miyoshi, Over 43%-power-efficiency GaInN-based photoelectric transducer on free-standing GaN substrate for optical wireless power transmission system, Semicond. Sci. Technol. **39**, 045010 (2024).

[5] Y. Xu, V. G. T. Vangipuram, V. Talesara, J. Cheng, Y. Zhang, T. Hashimoto, E. Letts, D. Key, H. Zhao, and W. Lu, 7.86 kV GaN-on-GaN PN power diode with $BaTiO_3$ for electrical field management, Appl. Phys. Lett. **123**, 142105 (2023).

[6] A. Udabe, I. Baraia-Etxaburu, and D. G. Diez, Gallium nitride power devices: A state of the art review, IEEE Access **11**, 48628 (2023).

[7] L. Cohen, J. B. Bernstein, and I. Aharon, Gate driver for high-frequency power converter, Electronics **14**, 224 (2025).

[8] P. Murugapandiyan, S. Maheswari, A. S. Augustine Fletcher, G. Saranya, and P. Anandan, Recent advancement in ScAlN/GaN high electron mobility transistors: Materials, properties, and device performance, Mater. Sci. Semicond. Process. **193**, 109509 (2025).

[9] B. M. Shi, M. H. Xi, H. S. Wu, N. Wang, and S. Y. Tong, Transition between wurtzite and zinc-blende GaN: An effect of deposition condition of molecular-beam epitaxy, Appl. Phys. Lett. **89**, 151921 (2006).

[10] D. J. As and K. Lischka, Nonpolar cubic III-nitrides: From the basics of growth to device applications, in *Molecular Beam Epitaxy From Research to Mass Production*, edited by M. Henini (Elsevier, 2018), Chap. 6, pp. 95–114.

[11] S. Kako, M. Holmes, S. Sergent, M. Bürger, D. J. As, and Y. Arakawa, Single-photon emission from cubic GaN quantum dots, Appl. Phys. Lett. **104**, 011101 (2014).

[12] S. Blumenthal, D. Reuter, and D. J. As, Optical properties of cubic GaN quantum dots grown by molecular beam epitaxy, Phys. Status Solidi B **255**, 1700457 (2018).

[13] R. Gao, G. Bian, H. Yuan, and H. Wang, Identification of the spintronic $Ni_{Ga}V_N$ center in c-GaN and its qubit applications, J. Phys. D: Appl. Phys. **54**, 505109 (2021).

[14] S. Kako, M. Miyamura, K. Tachibana, K. Hoshino, and Y. Arakawa, Size-dependent radiative decay time of excitons in GaN/AlN self-assembled quantum dots, Appl. Phys. Lett. **83**, 984 (2003).

[15] M. Bürger, T. Schupp, K. Lischka, and D. J. As, Cathodoluminescence spectroscopy of zinc-blende GaN quantum dots, Phys. Status Solidi C **9**, 1273 (2012).

[16] C. J. M. Stark, T. Detchprohm, S. C. Lee, Y.-B. Jiang, S. R. J. Brueck, and C. Wetzel, Green cubic GaInN/GaN light-emitting diode on microstructured silicon (100), Appl. Phys. Lett. **103**, 232107 (2013).

[17] S. Sergent, S. Kako, M. Bürger, T. Schupp, D. J. As, and Y. Arakawa, Polarization properties of single zinc-

blende GaN/AlN quantum dots, Phys. Rev. B **90**, 235312 (2014).

[18] S. Li, J. Schörmann, D. J. As, and K. Lischka, Room temperature green light emission from nonpolar cubic InGaN/GaN multi-quantum-wells, Appl. Phys. Lett. **90**, 071903 (2007).

[19] D. J. As and C. Mietze, MBE growth and applications of cubic AlN/GaN quantum wells, Phys. Status Solidi A **210**, 474 (2013).

[20] D. J. Binks, P. Dawson, R. A. Oliver, and D. J. Wallis, Cubic GaN and InGaN/GaN quantum wells, Appl. Phys. Rev. **9**, 041309 (2022).

[21] D. Dyer, S. A. Church, R. Ahumada-Lazo, M. J. Kappers, M. P. Halsall, P. Parkinson, D. J. Wallis, R. A. Oliver, and D. J. Binks, Efficiency droop in zincblende InGaN/GaN quantum wells, Nanoscale **16**, 13953 (2024).

[22] S. A. Jentsch, M. F. Zscherp, A. F. Campbell, M. Stein, M. Chia, D. J. As, J. Lähnemann, S. Chatterjee, and J. Schörmann, Cubic InGaN for red emission: Improved phase stability and emission properties by metal-modulated epitaxy, J. Appl. Phys. **138**, 225702 (2025).

[23] D. J. Binks, D. Dyer, W. R. Fieldhouse-Allen, and D. J. Wallis, Recent progress in cubic GaN epilayers and InGaN/GaN quantum wells, J. Phys. D: Appl. Phys. **59**, 253002 (2026).

[24] M. T. Durniak, A. S. Bross, D. Elsaesser, A. Chaudhuri, M. L. Smith, A. A. Allerman, S. C. Lee, R. J. Brueck, and C. Wetzel, Green emitting cubic GaInN/GaN quantum well stripes on micropatterned Si(001) and their strain analysis, Adv. Electron. Mater. **2**, 1500327 (2016).

[25] D. Schiavon, M. Binder, M. Peter, B. Galler, P. Drechsel, and F. Schulz, Wavelength-dependent determination of the recombination rate coefficients in single-quantum-well GaInN/GaN light emitting diodes, Phys. Status Solidi B **250**, 283 (2013).

[26] M. Auf der Maur, A. Pecchia, G. Penazzi, W. Rodrigues, and A. Di Carlo, Efficiency drop in green InGaN/GaN light emitting diodes: The role of random alloy fluctuations, Phys. Rev. Lett. **116**, 027401 (2016).

[27] E. Kioupakis, Q. Yan, and C. G. Van de Walle, Interplay of polarization fields and Auger recombination in the efficiency droop of nitride light-emitting diodes, Appl. Phys. Lett. **101**, 231107 (2012).

[28] Y.-S. Yoo, J.-H. Na, S. J. Son, and Y.-H. Cho, Effective suppression of efficiency droop in GaN-based light-emitting diodes: Role of significant reduction of carrier density and built-in field, Sci. Rep. **6**, 34586 (2016).

[29] A. Kasic, M. Schubert, T. Frey, U. Köhler, D. J. As, and C. M. Herzinger, Optical phonon modes and interband transitions in cubic $Al_xGa_{1-x}N$ films, Phys. Rev. B **65**, 184302 (2002).

[30] M. Röppischer, R. Goldhahn, G. Rossbach, P. Schley, C. Cobet, N. Esser, T. Schupp, K. Lischka, and D. J. As, Dielectric function of zinc-blende AlN from 1 to 20 eV: Band gap and van Hove singularities, J. Appl. Phys. **106**, 076104 (2009).

[31] M. Feneberg, M. Röppischer, C. Cobet, N. Esser, J. Schörmann, T. Schupp, D. J. As, F. Hörich, J. Bläsing, A. Krost, and R. Goldhahn, Optical properties of cubic GaN from 1 to 20 eV, Phys. Rev. B **85**, 155207 (2012).

[32] M. Landmann, E. Rauls, W. G. Schmidt, M. Röppischer, C. Cobet, N. Esser, T. Schupp, D. J. As, M. Feneberg, and R. Goldhahn, Transition energies and direct-indirect band gap crossing in zinc-blende $Al_xGa_{1-x}N$, Phys. Rev. B **87**, 195210 (2013).

[33] E. Baron, R. Goldhahn, M. Deppe, D. J. As, and M. Feneberg, Influence of the free-electron concentration on the optical properties of zincblende GaN up to 1×10^{20} cm^{-3}, Phys. Rev. Mater. **3**, 104603 (2019).

[34] E. Baron, M. Feneberg, R. Goldhahn, M. Deppe, F. Tacken, and D. J. As, Optical evidence of many-body effects in the zincblende $Al_xGa_{1-x}N$ alloy system, J. Phys. D: Appl. Phys. **54**, 025101 (2021).

[35] M. F. Zscherp, S. A. Jentsch, M. J. Müller, V. Lider, C. Becker, L. Chen, M. Littmann, F. Meier, A. Beyer, D. M. Hofmann, D. J. As, P. J. Klar, K. Volz, S. Chatterjee, and J. Schörmann, Overcoming the miscibility gap of GaN/InN in MBE growth of cubic $In_xGa_{1-x}N$, ACS Appl. Mater. Interfaces **15**, 39513 (2023).

[36] S. A. Jentsch, M. F. Zscherp, V. Lider, F. Winkler, A. Beyer, J. Belz, N. M. Gimbel, M. Stein, D. J. As, A. Henss, K. Volz, S. Chatterjee, and J. Schörmann, Metal-modulated growth of cubic, red-emitting InGaN layers and self-assembled InGaN/GaN quantum wells by molecular beam epitaxy, ACS Appl. Electron. Mater. **7**, 1891 (2025).

[37] M. F. Zscherp, S. A. Jentsch, V. Lider, M. Chia, A. Beyer, A. Henss, D. J. As, K. Volz, S. Chatterjee, and J. Schörmann, Mechanism of self-assembled cubic InGaN/GaN quantum well formation in metal-modulated molecular beam epitaxy, Cryst. Growth Des. **25**, 3793 (2025).

[38] X. Xu, D. Dyer, M. Frentrup, W. R. Fieldhouse-Allen, M. J. Kappers, G. Kusch, D. J. Wallis, R. A. Oliver, and D. J. Binks, Effect of buffer layer thickness on recombination in zincblende InGaN/GaN quantum wells, J. Phys. D: Appl. Phys. **58**, 475101 (2025).

[39] M. Feneberg, J. Nixdorf, M. D. Neumann, N. Esser, L. Artús, R. Cuscó, T. Yamaguchi, and R. Goldhahn, Ordinary dielectric function of corundumlike α-Ga_2O_3 from 40 meV to 20 eV, Phys. Rev. Mater. **2**, 044601 (2018).

[40] A. Schleife, M. D. Neumann, N. Esser, Z. Galazka, A. Gottwald, J. Nixdorf, R. Goldhahn, and M. Feneberg, Optical properties of In_2O_3 from experiment and first-principles theory: Influence of lattice screening, New J. Phys. **20**, 053016 (2019).

[41] N. Nepomniashchaia, V. Vetokhina, D. Chvostova, Z. Bryknar, A. Dejneka, and M. Tyunina, Low-temperature NIR-VUV optical constants of (001) $LaAlO_3$ crystal, Opt. Mater. Express **12**, 3081 (2022).

[42] N. Nepomniashchaia, O. Pacherova, T. Kocourek, A. Dejneka, and M. Tyunina, Spectroscopic ellipsometry of epitaxially stressed ferroelectric films, J. Appl. Phys. **137**, 014103 (2025).

[43] P. Schley, R. Goldhahn, A. T. Winzer, G. Gobsch, V. Cimalla, O. Ambacher, H. Lu, W. J. Schaff, M. Kurouchi, Y. Nanishi, M. Rakel, C. Cobet, and N. Esser, Dielectric function and van Hove singularities for In-rich $In_xGa_{1-x}N$ alloys: Comparison of N- and metal-face materials, Phys. Rev. B **75**, 205204 (2007).

[44] F. Bechstedt, J. Furthmüller, and J.-M. Wagner, Electronic and vibrational properties of group-III nitrides: *Ab initio* studies, Phys. Status Solidi C **0**, 1732 (2003).

[45] L. C. de Carvalho, A. Schleife, and F. Bechstedt, Influence of exchange and correlation on structural and electronic properties of AlN, GaN, and InN polytypes, Phys. Rev. B **84**, 195105 (2011).

[46] J. Rose, E. Baron, R. Goldhahn, M. F. Zscherp, S. A. Jentsch, S. Chatterjee, J. Schörmann, and M. Feneberg, Bandgaps in cubic

InGaN for the entire composition range including many-body effects, J. Appl. Phys. **137**, 243106 (2025).

[47] P. Schley, R. Goldhahn, C. Napierala, G. Gobsch, J. Schörmann, D. J. As, K. Lischka, M. Feneberg, and K. Thonke, Dielectric function of cubic InN from the mid-infrared to the visible spectral range, Semicond. Sci. Technol. **23**, 055001 (2008).

[48] R. Goldhahn, P. Schley, and M. Röppischer, *Ellipsometry of InN and Related Alloys in Indium Nitride and Related Alloys*, edited by T. D. Veal, C. F. McConville, and W. J. Schaff (CRC Press, Taylor & Francis Group, Boca Raton, FL, 2010), pp. 315–376.

[49] M. F. Zscherp, N. Mengel, D. M. Hofmann, V. Lider, B. Ojaghi Dogahe, C. Becker, A. Beyer, K. Volz, J. Schörmann, and S. Chatterjee, AlN buffer enhances the layer quality of MBE-grown cubic GaN on 3C-SiC, Cryst. Growth Des. **22**, 6786 (2022).

[50] D. A. G. Bruggeman, Berechnung verschiedener physikalischer Konstanten von heterogenen Substanzen III. Die elastischen Konstanten der quasiisotropen Mischkörper aus isotropen Substanzen, Ann. Phys. **416**, 636 (1935).

[51] See Supplemental Material at http://link.aps.org/supplemental/10.1103/d9pn-bys3 for details of surface roughness comparison between AFM and ellipsometry, for second derivative of the pbp-DF, for experimental data and pbp-fit for all samples, for the model analysis of the pbp-DF for all samples, and for CP-model parameters other than energy position for all samples.

[52] B. Johs, C. Herzinger, J. Dinan, A. Cornfeld, and J. Benson, Development of a parametric optical constant model for $Hg_{1-x}Cd_xTe$ for control of composition by spectroscopic ellipsometry during MBE growth, Thin Solid Films **313–314**, 137 (1998).

[53] C. M. Herzinger and B. D. Johs, Dielectric function parametric model, and method of use, U. S. Patent 5796983 (1998).

[54] T. Werninghaus, M. Friedrich, V. Cimalla, J. Scheiner, R. Goldhahn, Optical characterization of MBE grown cubic and hexagonal SiC films on Si(111), D. R. T. Zahn, and J. Pezoldt, Diam. Relat. Mater. **7**, 1385 (1998).

[55] J. Scheiner, R. Goldhahn, V. Cimalla, G. Ecke, W. Attenberger, J. K. M. Lindner, G. Gobsch, and J. Pezoldt, Spectroscopic ellipsometry studies of heteroepitaxially grown cubic silicon carbide layers on silicon, Mater. Sci. Eng. B **61–62**, 526 (1999).

[56] Ch. Zgheib, Ch. Förster, P. Weih, V. Cimalla, M. Kazan, P. Masri, O. Ambacher, and J. Pezoldt, Infrared ellipsometry of SiC/Si heterostructures with Ge modified interfaces, Thin Solid Films **455–456**, 183 (2004).

[57] J. Pezoldt, Ch. Zgheib, V. Lebedev, P. Masri, and O. Ambacher, Determination of strain and composition in SiC/Si and AlN/Si heterostructures by FTIR-ellipsometry, Superlattices Microstruct. **40**, 612 (2006).

[58] D. E. Aspnes, Direct verification of the third-derivative nature of electroreflectance spectra, Phys. Rev. Lett. **28**, 168 (1972).

[59] P. Lautenschlager, M. Garriga, L. Viña, and M. Cardona, Temperature dependence of the dielectric function and interband critical points in silicon, Phys. Rev. B **36**, 4821 (1987).

[60] C. C. Kim, J. W. Garland, H. Abad, and P. M. Raccah, Modeling the optical dielectric function of semiconductors: Extension of the critical-point parabolic-band approximation, Phys. Rev. B **45**, 11749 (1992).

[61] S. Berrah, A. Boukortt, and H. Abid, Optical properties of the cubic alloy (In, Ga)N, Physica E **41**, 701 (2009).

[62] T. Wethkamp, K. Wilmers, N. Esser, W. Richter, O. Ambacher, H. Angerer, G. Jungk, R. L. Johnson, and M. Cardona, Spectroscopic ellipsometry measurements of $Al_xGa_{1-x}N$ in the energy range 3-25 eV, Thin Solid Films **313–314**, 745 (1998).

[63] C. Buchheim, R. Goldhahn, M. Rakel, C. Cobet, N. Esser, U. Rossow, D. Fuhrmann, and A. Hangleiter, Dielectric function and critical points of the band structure for AlGaN alloys, Phys. Status Solidi B **242**, 2610 (2005).

[64] E. Sakalauskas, Ö. Tuna, A. Kraus, H. Bremers, U. Rossow, C. Giesen, M. Heuken, A. Hangleiter, G. Gobsch, and R. Goldhahn, Dielectric function and bowing parameters of InGaN alloys, Phys. Status Solidi B **249**, 485 (2012).

[65] T. J. Kim, J. J. Yoon, S. Y. Hwang, Y. W. Jung, T. H. Ghong, Y. D. Kim, H. J. Kim, and Y.-C. Chang, InAs critical-point energies at 22 K from spectroscopic ellipsometry, J. Appl. Phys. **97**, 171912 (2010).

[66] P. Lautenschlager, M. Garriga, S. Logothetidis, and M. Cardona, Interband critical points of CsaAs and their temperature dependence, Phys. Rev. B **35**, 9174 (1987).

[67] S. Zollner, M. Garriga, J. Kircher, J. Humlíček, and M. Cardona, Temperature dependence of the dielectric function and the interband critical-point parameters of GaP, Phys. Rev. B **48**, 7915 (1993).